IOP Publishing Journal of Physics: Condensed Matter
J. Phys.: Condens. Matter **32** (2020) 235501 (8pp) https://doi.org/10.1088/1361-648X/ab786d

In-gap states of magnetic impurity in quantum spin Hall insulator proximitized to a superconductor

Szczepan Głodzik[1] **and Tadeusz Domański**

Institute of Physics, M. Curie-Skłodowska University, 20-031 Lublin, Poland

E-mail: szglodzik@kft.umcs.lublin.pl and doman@kft.umcs.lublin.pl

Received 3 October 2019, revised 2 January 2020
Accepted for publication 20 February 2020
Published 12 March 2020

Abstract

We study in-gap states of a single magnetic impurity embedded in a honeycomb monolayer which is deposited on superconducting substrate. The intrinsic spin–orbit coupling induces the quantum spin Hall insulating (QSHI) phase gapped around the Fermi energy. Under such circumstances we consider the emergence of Shiba-like bound states driven by the superconducting proximity effect. We investigate their topography, spin-polarization and signatures of the quantum phase transition manifested by reversal of the local currents circulating around the magnetic impurity. These phenomena might be important for more exotic in-gap quasiparticles in such complex nanostructures as magnetic nanowires or islands, where the spin–orbit interaction along with the proximity induced electron pairing give rise to topological phases hosting the protected boundary modes.

Keywords: bound states, Yu-Shiba-Rusinov states, superconductivity

(Some figures may appear in colour only in the online journal)

1. Introduction

Even a tiny content of impurities introduced to insulating and semiconducting materials can tremendously affect their charge transport, contributing particle/hole carriers from the donor/acceptor level to the conduction/valence band. This is in contrast with completely opposite (destructive) effect played by the magnetic impurities in superconductors where they break the Cooper pairs, leading to formation of the bound Yu-Shiba-Rusinov (YSR) or briefly Shiba states inside the energy gap [1]. These in-gap states can eventually activate the charge transport in interfaces and heterostructures, owing to the anomalous particle-to-hole (or hole-to-particle) Andreev scattering mechanism [2]. In all such cases impurities are intimately related with existence of the subgap states, whose nature differs depending on the host material. One may hence ask, whether *there can be established any connection between such contrasting in-gap states of insulators and superconductors?*

A promising platform for addressing this question could be a graphene sheet deposited on *s*-wave superconducting substrate. Electrons of such carbon atoms layer reveal a number of unique properties. Besides their Dirac-like behavior, stemming simply from a honeycomb geometry, the intrinsic spin–orbit coupling (SOC) can induce the QSHI phase [3] with the spin currents circulating along its boundaries. Such effect has been experimentally observed in graphene randomly decorated with the dilute Bi_2Te_3 nanoparticles [4] and in a heterostructure, consisting of a monolayer of WTe_2 placed between two layers of hexagonal boron nitride which has revealed topological properties up to relatively high temperatures of about 100 K [5]. Further phenomena related with electron pairing arise when a graphene sheet is proximitized to superconducting material [6–11]. For instance, graphene deposited on aluminum films acquires superconductivity with the effective coherence length $\xi \simeq 400$ nm [11], whereas grown on rhenium it shows high transparency of the interface, with the induced pairing gap $\Delta = 330 \pm 10\,\mu$eV [8]. Upon introducing impurities into proximitized graphene, there emerge various in-gap states, manifesting either the topologically trivial or non-trivial phases [12]. Another system for investigating the bound states of magnetic impurities might be possible in bilayer graphene, where upon twisting the carbon

[1] The author to whom any correspondence to be addressed.

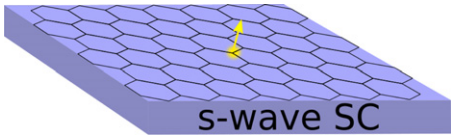

Figure 1. Scheme of a magnetic impurity embedded in a honeycomb monolayer and proximitized to *s*-wave superconductor.

sheets to a small 'magic' angle [13, 14] or tuning the interlayer coupling [15] the intrinsic unconventional superconducting phase is induced.

Here we investigate the properties of in-gap bound states formed at magnetic impurity embedded into the single honeycomb two-dimensional layer and proximitized to superconductor (figure 1), discussing feasible tools to unambiguously distinguish their Shiba-type character in presence of the QSHI phase. This problem has recently gained a great deal of interest, both experimentally [16–20] and theoretically [21–23] because similar magnetic structures, e.g. nanowires [24, 25] and nanostripes [26, 27] could enable realization of the Majorana quasiparticles.

The spin–orbit gap in graphene is often claimed to be rather small, although Sichau et al [28] have estimated its magnitude (by means of the resistively-detected electron spin resonance) to be 40 μeV. Under such circumstances the superconducting gap might be comparable to the SOC and this would be sufficient for appearance of the in-gap bound states strictly related with electron pairing. In what follows we perform a systematic study of the Shiba states, inspecting (a) their spatial extent and topography, (b) magnetic polarization, and (c) observable features of the quantum phase ($0-\pi$) transition manifested by reversal of the orbital currents circulating around the impurity site.

The paper is organized as follows. In section 2 we introduce the microscopic model and present the method for studying the bound states of magnetic impurity existing in honeycomb sheet. Section 3 discusses influence of the insulating and superconducting phases on the in-gap quasiparticles and presents their detailed properties. Finally, in section 4, we summarize the results.

2. Model and method

We describe the magnetic impurity embedded in a honeycomb sheet (figure 1) by the tight-binding Hamiltonian

$$\hat{H} = \hat{H}_{\rm imp} + \hat{H}_{K-M} + \hat{H}_{\rm Rashba} + \hat{H}_{\rm prox}. \tag{1}$$

In what follows, this impurity is treated classically

$$\hat{H}_{\rm imp} = -J\left(c^{\dagger}_{\mathbf{i}_0\uparrow}c_{\mathbf{i}_0\uparrow} - c^{\dagger}_{\mathbf{i}_0\downarrow}c_{\mathbf{i}_0\downarrow}\right), \tag{2}$$

where we denote the impurity site as $\mathbf{i}_0$, and we apply the Kane–Mele scenario [3] for description of the itinerant electrons

$$\begin{aligned}\hat{H}_{K-M} = &-t\sum_{\langle\mathbf{ij}\rangle\sigma\sigma'} c^{\dagger}_{\mathbf{i}\sigma}c_{\mathbf{j}\sigma} - \mu\sum_{\mathbf{i}\sigma} c^{\dagger}_{\mathbf{i}\sigma}c_{\mathbf{i}\sigma}\\ &+ i\lambda_{\rm SO}\sum_{\langle\langle\mathbf{ij}\rangle\rangle\sigma\sigma'} \nu_{\mathbf{ij}}c^{\dagger}_{\mathbf{i}\sigma}s_z^{\sigma\sigma'}c_{\mathbf{j}\sigma'},\end{aligned} \tag{3}$$

with the nearest-neighbor hopping t, the chemical potential μ (which we assume to be zero unless otherwise stated), and the imaginary, spin-dependent, next-nearest neighbor hopping amplitude $\lambda_{\rm SO}$. The latter term is responsible for inducing the helical edge states. The sign $\nu_{\mathbf{ij}} = \pm 1$ depends on the direction of electron hopping between the next-nearest-neighbor sites ($+1$ for clockwise and -1 for anticlockwise). The hopping terms involve the summation over (next-)nearest $\left(\langle\langle\mathbf{ij}\rangle\rangle\right)$ $\langle\mathbf{ij}\rangle$ neighbors. Since the substrate violates the mirror inversion $z \longrightarrow -z$ symmetry, we also consider the Rashba spin–orbit interactions

$$\hat{H}_{\rm Rashba} = i\lambda_R\sum_{\langle\mathbf{ij}\rangle\sigma\sigma'} c^{\dagger}_{\mathbf{i}\sigma}\left(\mathbf{s}^{\sigma\sigma'}\times\mathbf{d}_{\mathbf{ij}}\right)_{\vec{z}}c_{\mathbf{j}\sigma'}. \tag{4}$$

Here $\mathbf{s}^{\sigma\sigma'}$ is the vector of the Pauli matrices, referring to spin $\frac{1}{2}$, and the vector $\mathbf{d}_{\mathbf{ij}}$ connects site $\mathbf{i}$ with its nearest neighbor site $\mathbf{j}$.

Finally, we assume that the honeycomb layer is proximitized to *s*-wave superconductor

$$\hat{H}_{\rm prox} = \sum_{\mathbf{i}}\left(\Delta c^{\dagger}_{\mathbf{i}\uparrow}c^{\dagger}_{\mathbf{i}\downarrow} + \text{h.c.}\right), \tag{5}$$

which induces the on-site pairing Δ. For computing the observables of interest, we perform the Bogoliubov–Valatin transformation

$$c_{\mathbf{i}\sigma} = \sum_{n}{}' (u^{n}_{\mathbf{i}\sigma}\gamma_n - \sigma v^{*n}_{\mathbf{i}\sigma}\gamma^{\dagger}_n), \tag{6}$$

where $'$ denotes summation over the positive eigenvalues, and numerically solve the equations

$$\sum_{\mathbf{j}}\hat{H}_{\mathbf{ij}}\hat{\Phi}_{\mathbf{j}} = E_n\hat{\Phi}_{\mathbf{i}}, \tag{7}$$

in the auxiliary (Nambu spinor) representation $\Phi_{\mathbf{i}} = (u^{n}_{\mathbf{i}\uparrow}, u^{n}_{\mathbf{i}\downarrow}, v^{n}_{\mathbf{i}\uparrow}, v^{n}_{\mathbf{i}\downarrow})^{\rm T}$. The matrix elements read

$$\hat{H}_{\mathbf{ij}} = \begin{pmatrix} \tilde{t}_{\mathbf{ij}\uparrow} & \lambda_R^{\uparrow\downarrow} & 0 & \Delta \\ \lambda_R^{\downarrow\uparrow} & \tilde{t}_{\mathbf{ij}\downarrow} & \Delta & 0 \\ 0 & \Delta^{*} & -(\tilde{t}_{\mathbf{ij}\uparrow})^{*} & (\lambda_R^{\uparrow\downarrow})^{*} \\ \Delta^{*} & 0 & (\lambda_R^{\downarrow\uparrow})^{*} & -(\tilde{t}_{\mathbf{ij}\downarrow})^{*} \end{pmatrix}, \tag{8}$$

where $\tilde{t}_{\mathbf{ij}\sigma} = t_{\mathbf{j}}\delta_{\langle\mathbf{ij}\rangle} - (\mu + \sigma J\delta_{\mathbf{ii}_0})\delta_{\mathbf{ij}} + \sigma i\lambda_{\rm SO}\nu_{\mathbf{j}}\delta_{\langle\langle\mathbf{ij}\rangle\rangle}$ and $\lambda_R^{\sigma\sigma'}$ $= i\lambda_R\sum_{\sigma\sigma'\langle\mathbf{j}\rangle}\left(\mathbf{s}^{\sigma\sigma'}\times\mathbf{d}_{\mathbf{ij}}\right)_{\vec{z}} = (\lambda_R^{\sigma'\sigma})^{*}$.

Results discussed in this paper are obtained from numerical diagonalization of the Hamiltonian matrix on 40×40 lattice with the periodic boundary conditions in both directions. We do not consider any intrinsic pairing mechanism, assuming that it originates solely from the proximity effect (5). Self-consistent treatment of electron pairing is in general important [29, 30], however, in the present case it would not imply any significant changes of the local order parameter [31].

3. Subgap quasiparticles

For a systematic analysis of the subgap quasiparticles we shall start by discussing the in-gap states hosted in the insulating (QSHI) phase and next consider their mutation caused by the electron pairing Δ.

3.1. Impurity bound states in QSHI phase

Let us consider the magnetic impurity in a finite-size graphene layer, neglecting the superconducting substrate ($\Delta = 0$). Figure 2 shows how the intrinsic spin–orbit interaction affects the low-energy quasiparticles. We notice that insulating energy gap of the QSHI phase grows linearly upon increasing the Kane–Mele coupling and, around $\lambda_{\rm SO} = 0.2t$, it saturates to $\sim 1t$. Concomitantly there appear two in-gap states (purple-dotted lines in figure 2), which are fully spin-polarized. Similar bound states have been previously found for a single impurity whose magnetic moment is parallel to the graphene plane [32]. When impurity is close enough to a perimeter of the sample they have been shown to hybridize with the topological edge states, inducing antiresonances in the transmission matrix. It has been also emphasized, that the bound states around point impurity in a two-dimensional insulator could distinguish between the topological and trivial phases of the host material [33].

Bottom panel in figure 2 displays the topography of the occupied ($E < E_F$) bound state for two different values of $\lambda_{\rm SO}$. From careful examination of the spectral weight on the lattice sites adjacent to the impurity, we can notice an oscillatory decay of the wavefunction of the bound state. Practically its spatial extent does not exceed 10 atomic distances, and it quickly vanishes for higher magnitudes of the SOC. This loss of spatial extent is accompanied by the simultaneous reduction of the spectral weight of the bound state. Closely related effects have been previously pointed out for the magnetic [34–38], non-magnetic [12, 39, 40] and both types of the scattering potential as well [41–43].

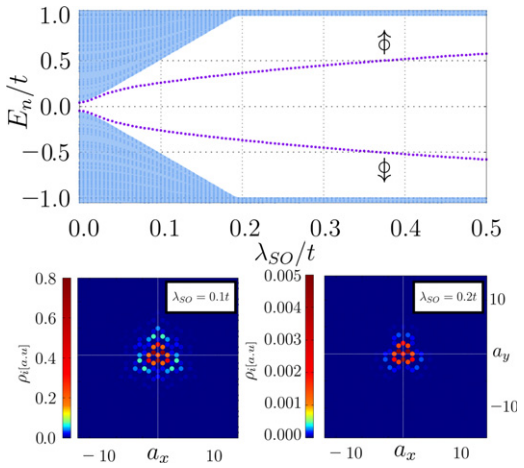

Figure 2. Low energy spectrum of the honeycomb lattice with the single magnetic impurity as a function of the Kane–Mele coupling $\lambda_{\rm SO}$, assuming $J = 6t$ and $\lambda_R = 0$, $\Delta = 0$. Bottom panel: topography of the occupied bound state for $\lambda_{\rm SO} = 0.1t$ and $\lambda_{\rm SO} = 0.2t$.

3.2. Shiba quasiparticles

Upon coupling the honeycomb lattice to superconducting substrate, the energy gap around the Fermi energy results from a combined effect of the proximity induced pairing ($\Delta \neq 0$) and the insulating phase. In general, these phenomena are known to be competitive as indeed manifested by suppression of the bulk order parameter $\langle c_{i\downarrow} c_{i\uparrow}\rangle$ (section 3.3). From a perspective of the local physics (at impurity site), however, relationship between the QSHI and superconducting phases is much more intriguing. By gradually increasing the pairing potential Δ, what can be achieved e.g. by reducing the external magnetic field or varying the temperature, we observe *development of the Shiba quasiparticles* [1] *directly from in-gap quasiparticles of the insulating phase* (figure 3). Let us remark, that direct transition from the insulating to superconducting phase has been theoretically considered for bulk materials within the mean field [44] and more sophisticated many-body methods [45]. Such scenario could be practically realized in variety of systems, e.g. thin superconducting films [46], at oxide interfaces [47],

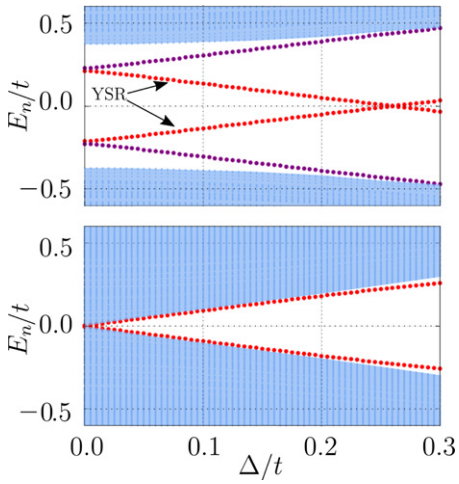

Figure 3. Top panel: emergence of YSR states (dotted red lines) from in-gap quasiparticles of the QSHI phase (dotted violet lines) driven by the proximity induced pairing Δ for $J = 6t$, $\lambda_{\rm SO} = 0.1t$, $\mu = 0$. Bottom panel: same but for $\mu = 3\sqrt{3}\lambda_{\rm SO}$.

in organic materials [48] and possibly in the doped cuprate superconductors [49]. In the present context we focus on the subgap Shiba-like quasiparticles, which to our knowledge have not been considered so far. To compare our results with less exotic situation, we plot in the bottom panel of figure 3 the same situation as in the top panel, but with a value of chemical potential which is known to close the spin–orbit gap. The system is then metallic and opening the superconducting gap results in a picture similar to traditionally understood Shiba states [1].

Let us focus in more detail on the Shiba quasiparticles. In the present case they do not obey the original formula $E_{\rm YSR} = \pm\Delta\,(1 - \pi\rho_n(E_F)J)\,/\,(1 + \pi\rho_n(E_F)J)$ derived for conventional superconductors because of the vanishing normal density of states in graphene $\rho_n(E_F) = 0$ [50, 51].

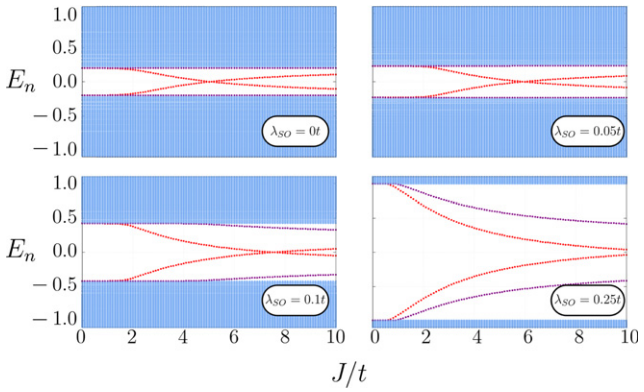

Figure 4. Evolution of the subgap spectrum with respect to the impurity potential J obtained for $\Delta = 0.2t$, $\lambda_R = 0.05t$ and several values of $\lambda_{\rm SO}$, as indicated. The dotted red and violet lines refer to the YSR states and in-gap quasiparticles of insulating phase, respectively.

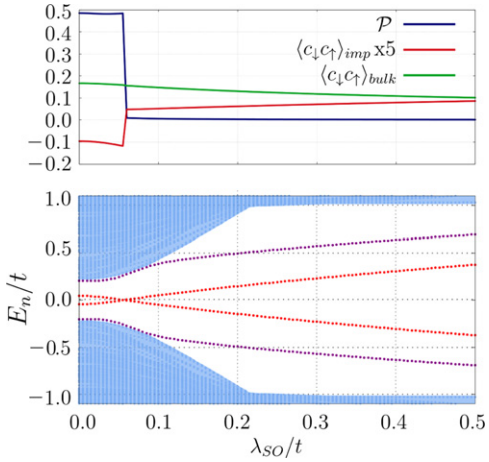

Figure 5. The polarization $\mathcal{P}$ and order parameter at the impurity site and for the bulk as functions of $\lambda_{\rm SO}$ (top panel). QPT driven at $\lambda_{\rm SO} \simeq 0.05t$ (bottom panel). Results obtained for the model parameters $\Delta = 0.2t$, $\lambda_R = 0.05t$, and $J = 6t$.

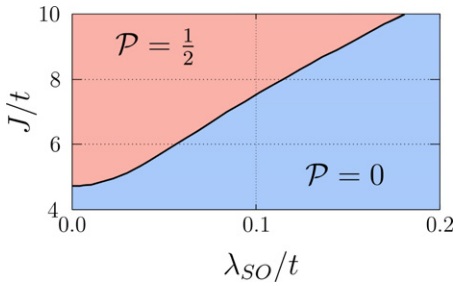

Figure 6. Variation of the QPT point (corresponding to crossing of the Shiba states) versus the Kane–Mele coupling $\lambda_{\rm SO}$ and impurity potential J.

Figure 4 displays the quasiparticle energies obtained numerically for our model as a function of the magnetic potential J for several values of Kane–Mele coupling $\lambda_{\rm SO}$. The dense (light-blue) dots refer to a continuum, whereas the single dotted lines represent the in-gap bound states. Amongst these in-gap branches we can recognize the Shiba-like quasiparticles by their strong variation with respect to J. In particular, at some critical value J_c they eventually cross each other, signaling a qualitative changeover of the ground state [52]. This quantum phase transition (QPT) manifests itself by: sign-reversal of the local order parameter ($0 - \pi$ transition), abrupt onset of the spin polarization (section 3.3), and by qualitative changes (both, in magnitude and vorticity) of the locally circulating currents (section 3.5).

Our analysis indicates, that Kane–Mele coupling $\lambda_{\rm SO}$ affects the QPT, by (i) shifting the critical coupling J_C to higher values (figures 4 and 6) and (ii) leading to substantial changes both in topography and spatial extent of the Shiba-like states (section 3.4). Thus the spin–orbit interaction weakens the efficiency of magnetic coupling J between the impurity and conduction electrons. Furthermore, the Shiba states no longer merge with a continuum even in the extremely strong coupling limit $J \to \infty$, in stark contrast to behavior of magnetic impurities in triangular lattice of the two-dimensional superconductor [21] where the Kane–Mele interaction is absent.

3.3. QPT

Let us now focus on the QPT, driven by the intrinsic SOC. Even though variation of $\lambda_{\rm SO}$ would be rather not feasible experimentally, we deem that its effect can be instructive for understanding mutual relationship between the on-site pairing and the spin–orbit interaction. Bottom panel of figure 5 presents the eigenenergies, corresponding to the same set of model parameters as in figure 2 but in presence of finite Δ and λ_R. We observe that energy gap of superconducting states ($\sim 0.2t$) gradually evolves into the gap of QSHI which saturates around $\lambda_{\rm SO} \simeq 0.2t$. We have selected strong enough magnetic coupling $J = 6t$ which allows for the QPT driven by $\lambda_{\rm SO}$. The upper panel of figure 5 displays the bulk polarization, defined as

$$\mathcal{P} = \frac{1}{2}\sum_{\mathbf{i}} \left(\langle n_{\mathbf{i}\uparrow}\rangle - \langle n_{\mathbf{i}\downarrow}\rangle\right), \tag{9}$$

where $n_{\mathbf{i}\sigma} = \sum_n' \left[|u^n_{\mathbf{i}\sigma}|^2 f(E_n,T) + |v^n_{\mathbf{i}\sigma}|^2 f(-E_n,T)\right]$ is the average number of electrons with spin σ at site $\mathbf{i}$, the order parameter at the impurity site, and its value averaged over the entire sample. At $\lambda_{\rm SO} \approx 0.05t$ the order parameter at impurity site reverses its sign and its absolute value gradually increases upon increasing the Kane–Mele coupling. Simultaneously the bulk magnetization is abruptly quenched as the system shifts to the unpolarized ground state. These characteristic features of the QPT [1] in the present case originate from the intrinsic SOC. On the other hand, the bulk order parameter does not undergo any dramatic changes (it slowly diminishes upon increasing $\lambda_{\rm SO}$). Such conditions should be taken into account when considering formation of the Majorana bound states at the ends of magnetic chains deposited on the proximitized honeycomb sheet [25].

The shift of J_c with increasing $\lambda_{\rm SO}$ is displayed as a phase diagram in figure 6. The black continuous line denotes the

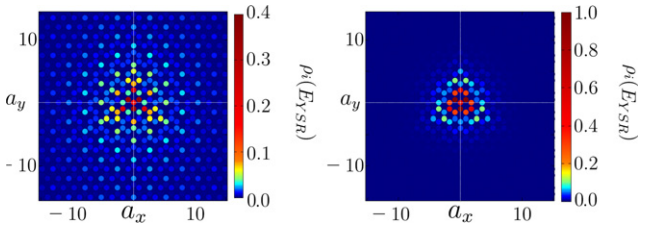

Figure 7. Spatial distribution of the occupied (negative value) Shiba quasiparticle obtained for $\Delta = 0.2t$, $\lambda_R = 0.05t$, $J = 4t$, using $\lambda_{SO} = 0$ (left panel) and $\lambda_{SO} = 0.1t$ (right panel). The density of states $\rho_i(E_{Shiba})$ is normalized with respect to the largest value in the bottom panel.

critical coupling J_c at different values of λ_{SO}. Initially the shift of QPT is not meaningful, but starting from $\lambda_{SO} = 0.03t$ we observe onset of a linear variation. This increase also points out, that the spin–orbit interaction suppresses the effective coupling of the impurity spin with the conduction electrons [36].

3.4. Topography of Shiba quasiparticles

Let us now inspect the real-space shape (topography) of the Shiba states. Figure 7 presents spatial maps of the density of states at the energy of electron-like (occupied) bound state, both in absence and in presence of the intrinsic spin–orbit interaction. One can see that without the Kane–Mele interaction, the topography of Shiba state has its usual character with exponential variation of the wavefunction $\sim \exp(-r/\xi)$.

We remark, that spectral weight is differently distributed in each sublattice. Close to the impurity site $r_0 = (0, 0)$ most of the spectral weight of the Shiba quasiparticles appears in the B-sublattice sites, whereas further away the A-sublattice (in which the impurity resides) gains more and more spectral weight. Also the rotational symmetry of the topographic shape reveals a bipartite character. Close to the impurity site the shape has a C_3 rotational symmetry, reflecting the fact that each site has three nearest-neighbors (cf bottom panels in figure 2), whereas at larger distances, the spectral weight distributed in the A sublattice resembles a hexagon with C_6 rotational symmetry. Precise evaluation of the bound states wavefuntions in this case would be a challenging task for future experimental measurements. Topography of the bound states changes dramatically, when the intrinsic SOC is taken into account. Bottom panel in figure 7 illustrates a strong tendency towards localization of the Shiba states in vicinity of the magnetic impurity. Their spectral weight is spread over a few adjacent sites and we no longer observe any preference for dominance of only one sublattice. These properties of the Shiba states resemble the features typical for in-gap quasiparticles of magnetic impurity embedded in a non-superconducting QSHI. Such reduction of the spatial extent could be important for engineering the topologically non-trivial phases, as e.g. chain of magnetic impurities can host the Majorana quasiparticles only when the bound states of dilute impurities hybridize to form a Shiba band capable of undergoing the topological phase transition.

3.5. Local currents

Another signature of the QPT in our system can be seen by currents induced around the magnetic impurity [53]. We compute the local charge flow, using the Heisenberg equation $i\hbar\frac{\partial\langle n_i\rangle}{\partial t} = \langle[n_i, \hat{H}]\rangle$. Setting the convention $\hbar \equiv 1$, and ignoring the terms which merely induce on-site fluctuations of charge, we obtain

$$\begin{aligned}\frac{\partial\langle n_{\mathbf{i}}\rangle}{\partial t} = &-it\sum_{\sigma\langle\mathbf{j}\rangle}\left(\langle c^{\dagger}_{\mathbf{i}\sigma}c_{\mathbf{j}\sigma}\rangle - \langle c^{\dagger}_{\mathbf{j}\sigma}c_{\mathbf{i}\sigma}\rangle\right)\\ &+\lambda_{SO}\sum_{\sigma\sigma'\langle\langle\mathbf{j}\rangle\rangle}\left(\nu_{\mathbf{ij}}s_z^{\sigma\sigma'}\langle c^{\dagger}_{\mathbf{i}\sigma'}c_{\mathbf{j}\sigma}\rangle - \nu_{\mathbf{ji}}s_z^{\sigma'\sigma}\langle c^{\dagger}_{\mathbf{j}\sigma'}c_{\mathbf{i}\sigma}\rangle\right)\\ &+\lambda_R\sum_{\sigma\sigma'\langle\mathbf{j}\rangle}\Big[\left(\mathbf{s}^{\sigma\sigma'}\times\mathbf{d}_{\mathbf{ij}}\right)_{\vec{z}}\langle c^{\dagger}_{\mathbf{i}\sigma}c_{\mathbf{j}\sigma'}\rangle\\ &-\left(\mathbf{s}^{\sigma'\sigma}\times\mathbf{d}_{\mathbf{ji}}\right)_{\vec{z}}\langle c^{\dagger}_{\mathbf{j}\sigma'}c_{\mathbf{i}\sigma}\rangle\Big].\end{aligned} \tag{10}$$

Applying the Bogoliubov–Valatin transformation (6), and making use of the fact that if $\Phi_{\mathbf{i}} = (u^n_{\mathbf{i}\uparrow}, u^n_{\mathbf{i}\downarrow}, v^n_{\mathbf{i}\uparrow}, v^n_{\mathbf{i}\downarrow})^{\mathrm{T}}$ is the eigenvector of matrix (8) with an eigenvalue E_n, then $\tilde{\Phi}_{\mathbf{i}} = (-v^{n*}_{\mathbf{i}\uparrow}, v^{n*}_{\mathbf{i}\downarrow}, -u^{n*}_{\mathbf{i}\uparrow}, u^{n*}_{\mathbf{i}\downarrow})^{\mathrm{T}}$ is also an eigenvector of the same matrix, but with an eigenvalue $-E_n$, we get

$$\begin{aligned}\langle\widehat{J}_{\mathbf{i}}\rangle = &-it\sum_{\langle\mathbf{j}\rangle\sigma n}\left(u^{n*}_{\mathbf{i}\sigma}u^{n}_{\mathbf{j}\sigma}f_{FD}(E_n) - \text{c.c.}\right)\\ &+\sum_{\langle\mathbf{j}\rangle\sigma\sigma' n}\left(\lambda_R^{\sigma\sigma'}u^{n*}_{\mathbf{i}\sigma}u^{n}_{\mathbf{j}\sigma'}f_{FD}(E_n) + \text{c.c.}\right)\\ &+\lambda_{SO}\sum_{\langle\langle\mathbf{j}\rangle\rangle\sigma\sigma' n}\left(\nu_{\mathbf{ij}}s_z^{\sigma\sigma'}u^{n*}_{\mathbf{i}\sigma}u^{n}_{\mathbf{j}\sigma'}f_{FD}(E_n) + \text{c.c.}\right),\end{aligned} \tag{11}$$

where $\lambda_R^{\sigma\sigma'}$ defined in section 2.

Figure 8 shows the real-space maps of microscopic currents and the maximum magnitude of bond current in the system with respect to the impurity coupling strength J. We emphasize, that reversal of these currents vorticity (compare the top panels of figure 8) occurs exclusively when the system is in the non-trivial QSHI phase. Explanation of this behavior could be the following. It has been shown in reference [36] that the intrinsic SOC supresses the effective coupling J of impurity with the conduction electrons. We have observed that with $\lambda_{SO} = 0$ the sites belonging to the same sublattice as the impurity site polarize easily in the direction of the magnetic moment of the impurity. This effect is pronounced only for $J > J_C$, as more sites around the impurity align their magnetic moments. The situation changes with increasing SOC which weakens the effective impurity coupling. For small J, the magnetic moment is hardly screened by the closest neighboring sites and becomes more efficient when the coupling exceeds the critical value J_C, forcing the neighboring sites to align their magnetization with the impurity. This in turn reverses the direction of the current. The Shiba states (labeled YSR in red vector plots in figure 8) are the ones that cross the Fermi energy during the QPT, hence only their contribution to the current shows this change of direction, in contrast to the bound states (BS in blue vector plots in figure 8) discussed in section 3.1. Those states hardly change their energy with increasing J, and their contribution to the current does not change during the QPT. Bottom

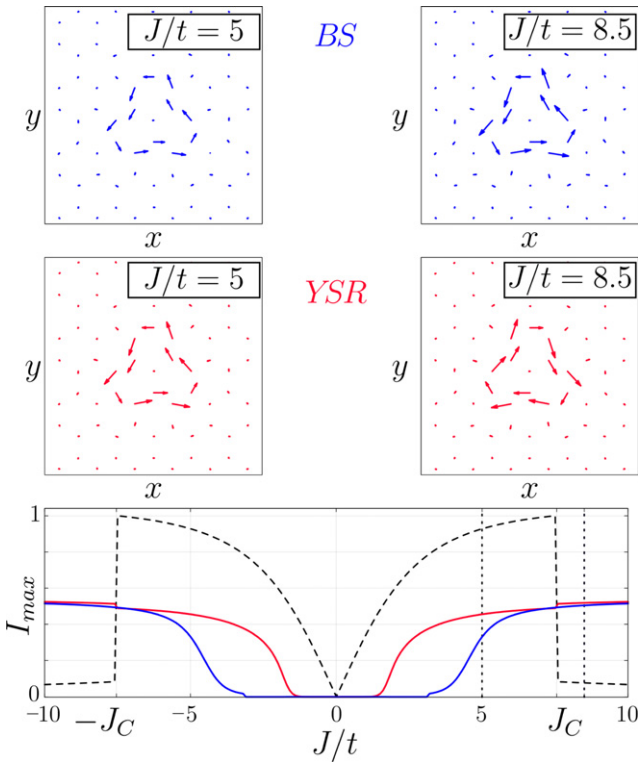

Figure 8. Vector maps of the currents around the magnetic impurity obtained for $J = 5t$ (left) and $J = 8.5t$ (right) presenting contributions of QSHI bound states (BS) and Shiba states (YSR). Bottom panel shows the maximum current versus the coupling J when taking into account the whole spectrum (black dashed line), only QSHI bound states and Shiba states (blue and red lines respectively). Other parameters: $\Delta = 0.2t$, $\lambda_{SO} = 0.1t$, $\lambda_R = 0.05t$.

panel in figure 8 presents the maximum value of the current in the system. When summing over every state n in equation (11), the current drops discontinuously at QPT. This is because as can be observed from the contribution of only the Shiba states (red) and the QSHI bound states (blue), after the reversal of current direction of the Shiba states, both contributions compete, and the effective maximum current is greatly reduced. Detection of such orbital patterns might be performed using an integrated quantum imaging platform where graphene sheet is connected to an array of the atomic-sized magnetic sensors [54, 55] or local conductivity atomic force microscopy suitable for probing electronic current paths with a diameter in the nanometer range [56].

4. Conclusions

We have theoretically investigated the energetic, magnetic and topographic features of in-gap quasiparticles of a single magnetic impurity embedded in the graphene sheet and proximitized to the superconducting substrate. We have shown that subtle interplay between the intrinsic spin–orbit interaction (responsible for the energy gap of the QSHI phase) and the proximity-induced electron pairing enables *emergence of the Shiba-type quasiparticles directly from in-gap states of the insulating phase*. We have discussed in detail this intriguing behavior and proposed several methods for its empirical verification.

Furthermore we have found, that upon varying either the magnetic coupling J (feasible in STM experiments [18]) or strength of the spin–orbit coupling λ_{SO} a pair of the Shiba bound states could cross at the Fermi energy, causing quantum phase transition of the ground state. This usually leads to sign-change of the local order parameter [1], but in the present situation it would be also uniquely manifested by a reversal of the vorticity and abrupt change of the absolute magnitude of the local currents circulating around the impurity site. Our numerical calculations have additionally revealed, that the spin–orbit coupling pushes such QPT crossing towards much higher values of J and substantially reduces the extent of Shiba states (similar to the in-gap states of insulating phase), partly affecting their topographic patterns. We have carefully inspected their spatial profiles in each sublattice of the graphene sheet.

We hope that phenomena discussed here for the single-site magnetic defects [57, 58] might stimulate further considerations of the topological insulating and/or superconducting phases in more complex magnetic structures, like nanowires [24, 25], nanoscopic islands [19] or stripes [26, 27], where the Majorana-type quasiparticles can be realized. It would be also worth to extend our study on the quantum impurities, addressing the subgap Kondo physics of the conventional [59, 60] and topological [61] superconductors.

Acknowledgments

This work was supported by National Science Center (NCN, Poland) under the grants 2017/27/N/ST3/01762 (S G) and UMO-2017/27/B/ST3/01911 (T D).

ORCID iDs

Szczepan Głodzik https://orcid.org/0000-0001-7928-9959
Tadeusz Domański https://orcid.org/0000-0003-1977-3989

References

[1] Balatsky A V, Vekhter I and Zhu J-X 2006 Impurity-induced states in conventional and unconventional superconductors *Rev. Mod. Phys.* **78** 373
[2] Heinrich B W, Pascual J I and Franke K J 2018 Single magnetic adsorbates on s-wave superconductors *Prog. Surf. Sci.* **93** 1
[3] Kane C L and Mele E J 2005 Quantum spin Hall effect in graphene *Phys. Rev. Lett.* **95** 226801
[4] Hatsuda K, Mine H, Nakamura T, Li J, Wu R, Katsumoto S and Haruyama J 2018 Evidence for a quantum spin hall phase in graphene decorated with Bi_2Te_3 nanoparticles *Sci. Adv.* **4**
[5] Wu S, Fatemi V, Gibson Q D, Watanabe K, Taniguchi T, Cava R J and Jarillo-Herrero P 2018 Observation of the quantum spin Hall effect up to 100 kelvin in a monolayer crystal *Science* **359** 76–9
[6] Heersche H B, Jarillo-Herrero P, Oostinga J B, Vandersypen L M K and Morpurgo A F 2007 Bipolar supercurrent in graphene *Nature* **446** 56–9
[7] Komatsu K, Li C, Autier-Laurent S, Bouchiat H and Guéron S 2012 Superconducting proximity effect in long

superconductor/graphene/superconductor junctions: From specular Andreev reflection at zero field to the quantum Hall regime *Phys. Rev. B* **86** 115412
[8] Tonnoir C, Kimouche A, Coraux J, Magaud L, Delsol B, Gilles B and Chapelier C 2013 Induced superconductivity in graphene grown on rhenium *Phys. Rev. Lett.* **111** 246805
[9] Han Z, Allain A, Arjmandi-Tash H, Tikhonov K, Feigelman M, Sacépé B and Bouchiat V 2014 Collapse of superconductivity in a hybrid tin–graphene Josephson junction array *Nat. Phys.* **10** 380
[10] Calado V E, Goswami S, Nanda G, Diez M, Akhmerov A R, Watanabe K, Taniguchi T, Klapwijk T M and Vandersypen L M K 2015 Ballistic Josephson junctions in edge-contacted graphene *Nat. Nanotechnol.* **10** 761
[11] Natterer F D, Ha J, Baek H, Zhang D, Cullen W G, Zhitenev N B, Young K and Stroscio J A 2016 Scanning tunneling spectroscopy of proximity superconductivity in epitaxial multilayer graphene *Phys. Rev. B* **93** 045406
[12] González J W and Fernández-Rossier J 2012 Impurity states in the quantum spin Hall phase in graphene *Phys. Rev. B* **86** 115327
[13] Cao Y, Fatemi V, Fang S, Watanabe K, Taniguchi T, Kaxiras E and Jarillo-Herrero P 2018 Unconventional superconductivity in magic-angle graphene superlattices *Nature* **556** 43
[14] Lu X *et al* 2019 Superconductors, orbital magnets and correlated states in magic-angle bilayer graphene *Nature* **574** 653
[15] Yankowitz M, Chen S, Polshyn H, Zhang Y, Watanabe K, Taniguchi T, Graf D, Young A F and Dean C R 2019 Tuning superconductivity in twisted bilayer graphene *Science* **363** 1059 https://science.sciencemag.org/content/363/6431/1059.full.pdf
[16] Ménard G C *et al* 2015 Coherent long-range magnetic bound states in a superconductor *Nat. Phys.* **11** 1013
[17] Hatter N, Heinrich B W, Rolf D and Franke K J 2017 Scaling of Yu-Shiba-Rusinov energies in the weak-coupling Kondo regime *Nat. Commun.* **8** 2016
[18] Farinacci L, Ahmadi G, Reecht G, Ruby M, Bogdanoff N, Peters O, Heinrich B W, von Oppen F and Franke K J 2018 Tuning the coupling of an individual magnetic impurity to a superconductor: quantum phase transition and transport *Phys. Rev. Lett.* **121** 196803
[19] Ménard G C, Brun C, Leriche R, Trif M, Debontridder F, Demaille D, Roditchev D, Simon P and Cren T 2019 Yu-Shiba-Rusinov bound states versus topological edge states in Pb/Si(111) *Eur. Phys. J. Special Topics* **227** 2303–13
[20] Kezilebieke S, Dvorak M, Ojanen T and Liljeroth P 2018 Coupled Yu-Shiba-Rusinov states in molecular dimers on $NbSe_2$ *Nano Lett.* **18** 2311–5
[21] Ptok A, Głodzik S and Domański T 2017 Yu-Shiba-Rusinov states of impurities in a triangular lattice of $NbSe_2$ with spin-orbit coupling *Phys. Rev. B* **96** 184425
[22] Körber S, Trauzettel B and Kashuba O 2018 Collective Yu-Shiba-Rusinov states in magnetic clusters at superconducting surfaces *Phys. Rev. B* **97** 184503
[23] Senkpiel J *et al* 2019 Robustness of Yu-Shiba-Rusinov resonances in the presence of a complex superconducting order parameter *Phys. Rev. B* **100** 014502
[24] Christensen M H, Schecter M, Flensberg K, Andersen B M and Paaske J 2016 Spiral magnetic order and topological superconductivity in a chain of magnetic adatoms on a two-dimensional superconductor *Phys. Rev. B* **94** 144509
[25] Teixeira R L R C, Kuzmanovski D, Black-Schaffer A M and Dias da Silva L G G V 2019 Gap oscillations and Majorana bound states in magnetic chains on superconducting honeycomb lattices *Phys. Rev. B* **99** 035127
[26] Fornieri A *et al* 2019 Evidence of topological superconductivity in planar Josephson junctions *Nature* **569** 89
[27] Ren H *et al* 2019 Topological superconductivity in a phase-controlled Josephson junction *Nature* **569** 93
[28] Sichau J, Prada M, Anlauf T, Lyon T J, Bosnjak B, Tiemann L and Blick R H 2019 Resonance microwave measurements of an intrinsic spin-orbit coupling gap in graphene: A possible indication of a topological state *Phys. Rev. Lett.* **122** 046403
[29] Meng T, Klinovaja J, Hoffman S, Simon P and Loss D 2015 Superconducting gap renormalization around two magnetic impurities: From Shiba to Andreev bound states *Phys. Rev. B* **92** 064503
[30] Hoffman S, Klinovaja J, Meng T and Loss D 2015 Impurity-induced quantum phase transitions and magnetic order in conventional superconductors: Competition between bound and quasiparticle states *Phys. Rev. B* **92** 125422
[31] Black-Schaffer A M 2011 Self-consistent superconducting proximity effect at the quantum spin Hall edge *Phys. Rev. B* **83** 060504
[32] Zheng J H and Cazalilla M A 2018 Nontrivial interplay of strong disorder and interactions in quantum spin-Hall insulators doped with dilute magnetic impurities *Phys. Rev. B* **97** 235402
[33] Slager R J, Rademaker L, Zaanen J and Balents L 2015 Impurity-bound states and Green's function zeros as local signatures of topology *Phys. Rev. B* **92** 085126
[34] Maciejko J, Liu C, Oreg Y, Qi X-L, Wu C and Zhang S-C 2009 Kondo effect in the helical edge liquid of the quantum spin Hall state *Phys. Rev. Lett.* **102** 256803
[35] Goth F, Luitz D J and Assaad F F 2013 Magnetic impurities in the Kane–Mele model *Phys. Rev. B* **88** 075110
[36] Hu F M, Wehling T O, Gubernatis J E, Frauenheim T and Nieminen R M 2013 Magnetic impurity affected by spin–orbit coupling: Behavior near a topological phase transition *Phys. Rev. B* **88** 045106
[37] Liu Q, Liu C-X, Xu C, Qi X-L and Zhang S-C 2009 Magnetic impurities on the surface of a topological insulator *Phys. Rev. Lett.* **102** 156603
[38] Zyuzin A A and Loss D 2014 RKKY interaction on surfaces of topological insulators with superconducting proximity effect *Phys. Rev. B* **90** 125443
[39] Lee H-H, Liu J-Y, Chang C-R and Shen S-Q 2013 Impurity influence in quantum spin Hall transport *Phys. Rev. B* **88** 195149
[40] Black-Schaffer A M and Balatsky A V 2012 Strong potential impurities on the surface of a topological insulator *Phys. Rev. B* **85** 121103
[41] Sessi P *et al* 2016 Dual nature of magnetic dopants and competing trends in topological insulators *Nat. Commun.* **7** 12027
[42] Biswas R R and Balatsky A V 2010 Impurity-induced states on the surface of three-dimensional topological insulators *Phys. Rev. B* **81** 233405
[43] Black-Schaffer A M, Balatsky A V and Fransson J 2015 Filling of magnetic-impurity-induced gap in topological insulators by potential scattering *Phys. Rev. B* **91** 201411
[44] Nozières P and Pistolesi F 1999 From semiconductors to superconductors: a simple model for pseudogaps *Eur. Phys. J. B* **10** 649–62
[45] Loh Y L, Randeria M, Trivedi N, Chang C-C and Scalettar R 2016 Superconductor-insulator transition and Fermi-Bose crossovers *Phys. Rev. X* **6** 021029
[46] Yazdani A and Kapitulnik A 1995 Superconducting-insulating transition in two-dimensional *a*-MoGe thin films *Phys. Rev. Lett.* **74** 3037
[47] Caviglia A D, Gariglio S, Reyren N, Jaccard D, Schneider T, Gabay M, Thiel S, Hammerl G, Mannhart J and Triscone J-M 2008 Electric field control of the $LaAlO_3/SrTiO_3$ interface ground state *Nature* (*London*) **456** 624–7
[48] Kanoda K and Kato R 2011 Mott physics in organic conductors with triangular lattices *Annu. Rev. Condens. Matter Phys.* **2** 167–88
[49] Bollinger A T, Dubuis G, Yoon J, Pavuna D, Misewich J and Bozovic I 2011 Superconductor–insulator transition in

$La_{2-x}Sr_xCuO_4$ at the pair quantum resistance *Nature* (*London*) **472** 458–60

[50] Lado J L and Ferněndez-Rossier J 2016 Unconventional Yu-Shiba-Rusinov states in hydrogenated graphene *2D Mater.* **3** 025001

[51] Wehling T O, Dahal H P, Lichtenstein A I and Balatsky A V 2008 Local impurity effects in superconducting graphene *Phys. Rev. B* **78** 035414

[52] Sakurai A 1970 Comments on superconductors with magnetic impurities *Prog. Theor. Phys.* **44** 1472

[53] Pershoguba S S, Björnson K, Black-Schaffer A M and Balatsky A V 2015 Currents induced by magnetic impurities in superconductors with spin-orbit coupling *Phys. Rev. Lett.* **115** 116602

[54] Tetienne J-P, Dontschuk N, Broadway D A, Stacey A, Simpson D A and Hollenberg L C L 2017 Quantum imaging of current flow in graphene *Sci. Adv.* **3**

[55] Casola F, van der Sar T and Yacoby A 2018 Probing condensed matter physics with magnetometry based on nitrogen-vacancy centres in diamond *Nat. Rev. Mater.* **3** 17088

[56] Rodenbücher C, Bihlmayer G, Speier W, Kubacki J, Wojtyniak M, Rogala M, Wrana D, Krok F and Szot K 2018 Local surface conductivity of transition metal oxides mapped with true atomic resolution *Nanoscale* **10** 11498

[57] Yazyev O V and Helm L 2007 Defect-induced magnetism in graphene *Phys. Rev. B* **75** 125408

[58] Lopez-Bezanilla A and Lado J L 2019 Defect-induced magnetism and Yu-Shiba-Rusinov states in twisted bilayer graphene *Phys. Rev. Mater.* **3** 084003

[59] Bauer J, Oguri A and Hewson A C 2007 Spectral properties of locally correlated electrons in a Bardeen–Cooper–Schrieffer superconductor *J. Phys.: Condens. Matter* **19** 486211

[60] Liu C, Huang Y, Chen Y and Ting C S 2019 Temperature-dependent spectral function of a Kondo impurity in an *s*-wave superconductor *Phys. Rev. B* **99** 174502

[61] Wang R, Su W, Zhu J-X, Ting C S, Li H, Chen C, Wang B and Wang X 2019 Kondo signatures of a quantum magnetic impurity in topological superconductors *Phys. Rev. Lett.* **122** 087001